Geophysical Research Letters

RESEARCH LETTER
10.1029/2020GL090165

Alpha Transmitter Signal Reflection and Triggered Emissions

Wenyao Gu[1], Lunjin Chen[1], Zhiyang Xia[1], Xin An[2], and Richard B. Horne[3]

[1]Physics Department, W. B. Hanson Center for Space Sciences, University of Texas at Dallas, Richardson, TX, USA, [2]Department of Atmospheric and Oceanic Sciences, University of California, Los Angeles, CA, USA, [3]British Antarctic Survey, Cambridge, UK

Key Points:
- Both ducted reflected signals and triggered emissions from transmitters are observed in the magnetosphere
- Ducted propagation is confirmed using time delay analysis and ray tracing model
- The interaction region for nonlinear growth is determined to be off the equator

Supporting Information:
- Supporting Information S1

Correspondence to:
W. Gu and L. Chen,
wxg170330@utdallas.edu;
lunjin.chen@gmail.com

Citation:
Gu, W., Chen, L., Xia, Z., An, X., & Horne, R. B. (2020). Alpha transmitter signal reflection and triggered emissions. *Geophysical Research Letters*, *47*, e2020GL090165. https://doi.org/10.1029/2020GL090165

Received 3 AUG 2020
Accepted 4 NOV 2020
Accepted article online 16 NOV 2020

Abstract Russian Alpha radio navigation system (RSDN-20) emits $F_1 = 11.9$ kHz signals into the magnetosphere which propagate as whistler mode waves. Observed by waveform continuous burst mode from Electric and Magnetic Field Instrument Suite and Integrated Science (EMFISIS) on Van Allen Probes, a case is presented and featured with ducted propagation, multiple reflections, and triggered emissions. Both risers and fallers appear in the triggered emissions. We use a ray tracing method to demonstrate ducted propagation, which has a similar wave normal angle near 150° as the observation. The arrival time of reflected signals is estimated using propagation analysis and compared with the observed signal arrival time. To test the nonlinear cyclotron resonance theory, the interaction region scale and the order of chirping rate in triggered emission are estimated. The estimated interaction region scale of MLAT = −3° is smaller than the observed MLAT = −6°. The discrepancy may be caused by the parallel propagation assumption and background field model.

1. Introduction

Signals from VLF transmitters can penetrate the ionosphere inside the transmitter cone and propagate in the magnetosphere in whistler mode, either ducted (Helliwell, 1965) or nonducted (Cerisier, 1973). In ducted propagation, signals propagate along the field line with nearly parallel wave normal angles. Such propagation requires one-sided or two-sided density structures (Helliwell, 1965) and generally has an upper cutoff frequency of *fce*/2 (half of electron gyrofrequency) (Smith, 1961). In nonducted propagation, the wave normal angle can become oblique and even nearly perpendicular. Reflection happens when wave frequency $f < f_{LHR}$ (lower hybrid resonance frequency) (Edgar, 1972; Kimura, 1966; Kulkarni et al., 2015). Bell et al. (1981) find continuous characteristics of in situ spatial, amplitude, and time delay distributions of signals and use them as evidences of nonducted waves. Comparing the in situ observation and the ray tracing group time delays, Rastani et al. (1985) identifies ducted and nonducted transmitter signals. Statistical studies on signal intensities by DEMETER (Clilverd et al., 2008; Zhang et al., 2018), CREES (Clilverd et al., 2008) and Van Allen Probes (Ma et al., 2017; Zhang et al., 2018) show that nonducted propagation dominates at $L < 1.5$, but there is still controversy on the dominant propagation mode in higher L shells (Agapitov et al., 2014; Ma et al., 2017; Zhang et al., 2018). We need more direct evidence on in situ wave normal angles to further study ducted and nonducted modes.

Cerisier (1973) indirectly derives in situ wave normal of transmitter signals using Doppler shift observed by FR-1 on 750 km altitude to demonstrate nonducted propagation. For higher-altitude observations, Sonwalkar and Inan (1986) use one electric dipole and one magnetic loop antenna to solve the wave normal based on the spinning of DE 1 satellite. With three orthogonal components of magnetic field measurement, Yamamoto et al. (1991) and Kimura et al. (2001) determine the wave normal from Akebono satellite using the technique by Means (1972). In this paper, we use the SVD (singular value decomposition) technique proposed by Santolík et al. (2003) to evaluate the wave normal angle observed by Van Allen Probes.

Triggered emissions of transmitter signals are observed both from ground stations (Carpenter & Miller, 1976; Golkowski et al., 2010, 2019; Helliwell, 1965; Helliwell & Katsufrakis, 1974; Li et al., 2015) and in space (Bell et al., 1981) with risers, fallers, and hooks in the dynamic spectrum. The phenomenon is interpreted by nonlinear cyclotron resonance when electrons are trapped to form an electron hole or hill (clump) in phase space (Omura et al., 1991, 2008), which is supported by numerical simulations (Hikishima et al., 2010;

Harid et al., 2014). Risers are thought to be generated with an electron hole while fallers are generated with an electron hill (Nunn & Omura, 2012; Tao et al., 2020; Wu et al., 2020; Wang & Berk, 2012; Yamaguchi et al., 2013).

The observation of ducted propagation accompanied by wave normal characteristics of multiple ducted signals is rarely available in the equatorial magnetosphere. In this paper, we present an event of Alpha transmitter signals in the magnetosphere by Van Allen Probes, revealing detailed features associated with ducted propagation. Then a ray tracing model is used to demonstrate the ducted propagation of the transmitter signal. This event, also accompanied with triggered emissions, provides a unique opportunity to test nonlinear cyclotron resonance theory by Omura et al. (2008).

2. Methodology

2.1. Alpha Transmitters

The Russian Alpha radio navigation system (RSDN-20) consists of three stations close to Krasnodar (45°24′N, 38°9′E), Novosibirsk (55°45′N, 84°27′E), and Khabarovsk (50°4′N, 136°36′E) (Jacobsen, 2006). The stations operate at three frequencies: $F_1 = 11.90$ kHz, $F_2 = 12.65$ kHz, and $F_3 = 14.88$ kHz. There is a unique pattern for each station at each frequency, with 0.4 s signal and 3.6 s period. Alpha transmitter signals at $L \sim 2$ are observed from ground via ducted propagation (Tanaka, Nishino, et al., 1987) and in space as nonducted propagation (Tanaka, Lagoutte, et al., 1987). From the statistical observations by DEMETER satellite at an altitude of 660 km, the maximum intensities of Alpha signals locate southward of the stations because of field line inclination (Zhang et al., 2017). For F_1 frequency, the nighttime amplitude near the conjugate points in the Southern Hemisphere is found to be lower than that above the transmitters (Vavilov et al., 2013). It has been proposed by Vavilov et al. (2013) and Zhang et al. (2017) that this phenomenon is due to the magnetospheric reflection above DEMETER orbit (660 km) for nonducted waves, where the local LHR frequency is higher than F_1 frequency.

2.2. Instrumentation and Data

The Van Allen Probes (formerly Radiation Belt Storm Probes, RBSP) are two spacecrafts orbiting near the Earth's equatorial plane with 600 km perigee, 30,000 km apogee, and 10° inclination angle. Their waveform continuous burst mode on Electric and Magnetic Field Instrument Suite and Integrated Science (EMFISIS) instrument provides continuous 6 s measurement on three orthogonal magnetic and electric field in UVW coordinates with a sampling rate of 35 kHz (Kletzing et al., 2013). The UVW coordinate system is defined in Kirby et al. (2014): $+W$ direction is toward the spin axis and $+U$ direction points to the nominal direction of EFW (the Electric Field and Waves Instrument) SPB (spin plane boom) ♯1; $+V$ direction is defined by the right-hand rule. However, a bandpass filter on the instrument completely attenuates F_3 frequency signals and partly attenuates F_2 frequency pulses (Koronczay et al., 2018). Therefore, we mainly focus on the wave observation at F_1 frequency. Figure 1 shows power spectral density of wave electric and magnetic fields captured by the burst mode EMFISIS waveform measurement, illustrating a typical example of Alpha signals in the magnetosphere. The power spectral density is obtained over the 6 s through window Fourier transformation with time window of 0.03 s and time shift of 0.015 s. The signals are from the Novosibirsk station due to the proximity of magnetic longitudes between the satellite location and the transmitter (within 1°). Three components of magnetic field are used in power spectral density calculation, while only EU and EV are used in electric power spectral density calculation due to the large uncertainties in EW component (Wygant et al., 2013). As shown in Figure 1, the 6 s waveform is capable of detecting the two pulses separated by 3.2 s. Therefore, Alpha signals at F_1 frequency can be recognized according to the pattern of pulses with 0.4 s duration and 3.2 s separation. The F_2 signals, which are attenuated by the instrument, also follow the same pattern except with a 0.6 s lag behind the F_1 signals, which is a characteristic of NOV station signals (Jacobsen, 2006). Wave normal angle, ellipticity and planarity are calculated by the SVD method using six components of the electromagnetic field (Santolík et al., 2003). The sign of parallel component of wave vector is decided by the direction of the Poynting vector. We also use Van Allen Probes L4 electron density data, which is inferred from the upper hybrid band (Kurth et al., 2015).

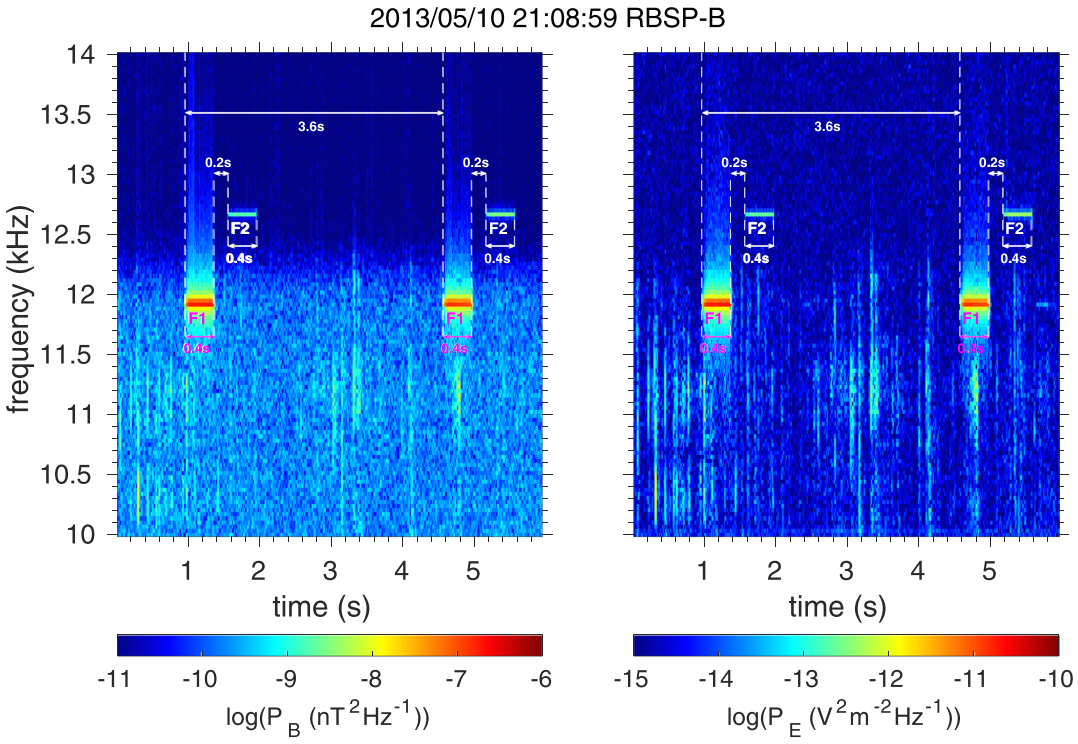

Figure 1. An example of alpha transmitter signals received by RBSPB satellite. The left panel shows the magnetic power spectrum, and the right panel shows the electric power spectrum. $F_1 = 11.9$ kHz signals and attenuated $F_2 = 12.7$ kHz signals are shown. White dashed lines show the starting times of the F_1 signals. The two F_1 signals show the pattern: 0.4 s signals with 3.6 s period. The F_2 signals lag 0.6 s behind the F_1 signals. The case is observed at $L = 2.7$, MLAT $= -0.1°$, and MLON $= 161.9°$, close to magnetic longitude of Novosibirsk (NOV) station at MLON $= 161.1°$.

3. Observation

Figure 2 shows an observation case of Alpha transmitter signals on UT 17:37 14 November 2012 (marked by the vertical red lines), which includes a 6 s waveform starting at 37:52.7 (mm:ss) and a 1 s segment of the previous consecutive waveform. The case occurs just after the recovery phase of a geomagnetic disturbance with SYM-H index variation shown in Figure 2a. The satellite locates inside the plasmasphere of electron density >100 cm^{-3} (Figure 2b) and of plasmapause location near $L \sim 3$. The electron cyclotron frequency f_{ce} is 140 kHz and the lower hybrid frequency $f_{LHR} \approx \sqrt{f_{ce} f_{ci}} = 3.2$ kHz, where f_{ci} is the ion cyclotron frequency. The Fourier analysis of the electromagnetic waveform data (Figures 2c and 2d) collected at this time (corresponding to magnetic local time ~23.7) shows distinct signal pulses occur at F_1 and F_2 frequencies. Each of them lasts 0.4 s, and the separation of the two F_2 pulses are about 3.2 s, all of which are consistent with the known Alpha transmitter signal pattern. The case locates at magnetic longitude (MLON) ~160.9°, which is close to the magnetic longitude of NOV station (MLON = 161.1°), so the signals are emitted from the NOV transmitter. It is interesting to note that, unlike the usual pattern shown in Figure 1, there are more F_1 pulses than F_2 pulses (probably because of the instrument attenuation at F_2 frequencies) and F_1 pulses are separated less than 3.2 s. The propagation characteristics are shown in Figures 2e–2j using the SVD method. One can see all the F_1 and F_2 pulses have positively high ellipticity (Figure 2e) and high planarity (Figure 2f), supporting that they are whistler mode waves. The ellipticity and planarity values for all the pulses are shown in Table 1. Wave normal vector direction (Figure 2g) alternates from antiparallel (or southward direction with $\theta_k = 180°$) and parallel (or northward direction with $\theta_k = 0°$) propagation, where θ_k is polar angle of wave vector with respect to the background magnetic field. The same is true for Poynting vector polar angle θ_p (Figure 2i). Such alternation of wave normal and Poynting vector directions suggest there exists multiple reflections. Based on the known Alpha transmitter signal pattern and wave normal variation of the pulses, there would be the only interpretation to connecting those pulses below. Therefore, we identify the F_1 signals at 37:51.9 (mm:ss) and 37:55.5 (mm:ss) as the original signals from the station that

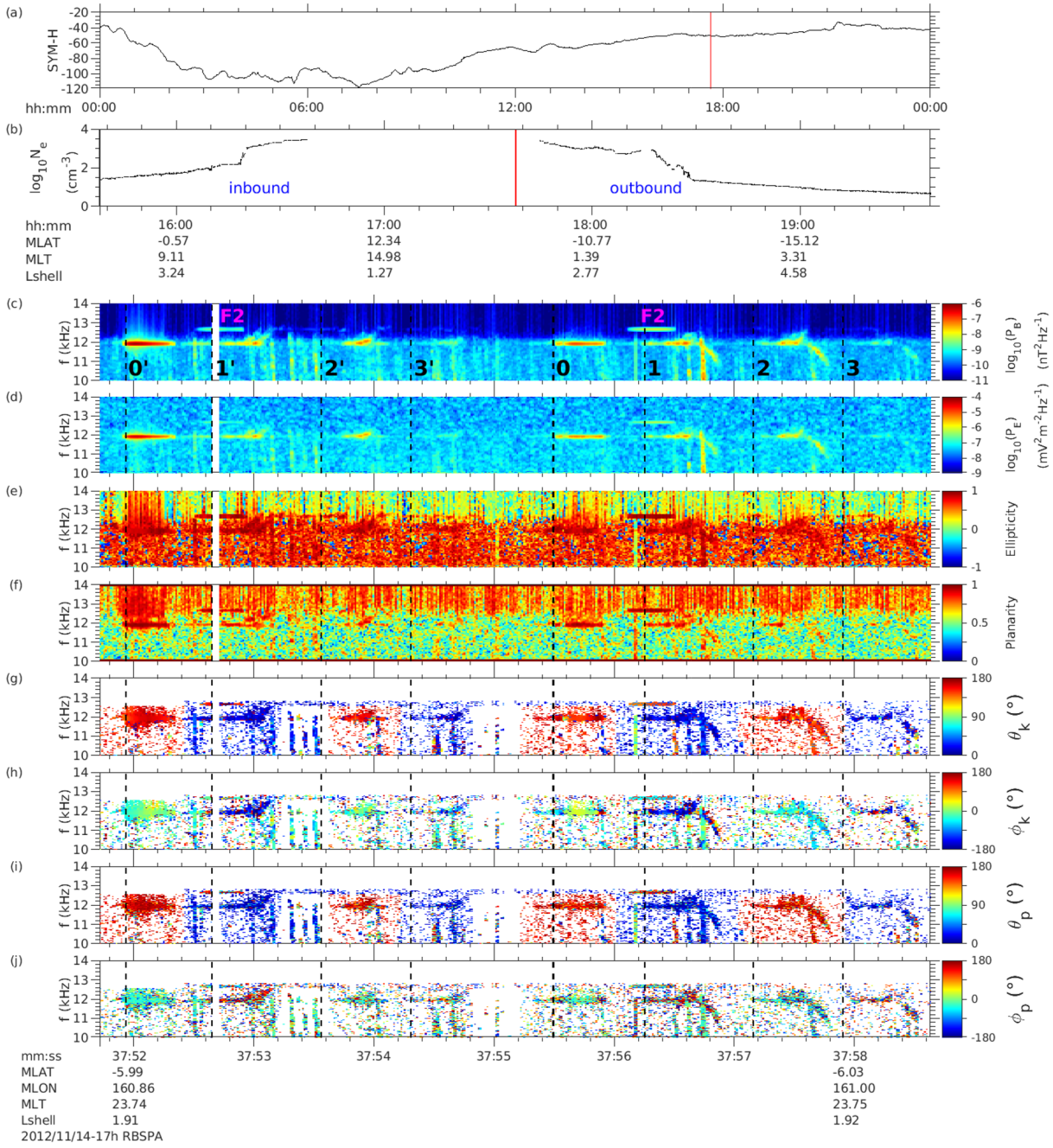

Figure 2. Alpha transmitter signals observed by RBSPA on 14 November 2012. (a) SYM-H of the day. The red line shows the time of the case. (b) Electron density. The red line shows the time of the case. (c) Magnetic field power. (d) Electric field power. (e) Ellipticity. (f) Planarity. (g) Polar angle of k vector. (h) Azimuthal angle of k vector. 0° stands for radially outward. (i) Polar angle of Poynting vector. (j) Azimuthal angle of Poynting vector; 0° stands for radially outward. The signal start times are labeled by black dash lines. F_2 signals and the reflection sequences of F_1 signals are noted in subplot (c).

propagate southward, which are labeled by 0′ and 0 in Figure 2c. The signals by 1 and 1′ have been reflected once from the conjugate point in the Southern Hemisphere and propagate northward. The signals labeled as 2 and 2′ have been reflected for the second time (from the Northern Hemisphere) and propagate southward. Similarly, the signals labeled 3 and 3′ have been reflected for the third time (from the Southern Hemisphere) and propagate northward. The labels without and with a prime denote two series of original and reflected signals, as the F_1 signals are 0.6 s ahead of F_2 signals in the NOV station (Jacobsen, 2006). Such categorization of the two series is also consistent with observation in Figures 2c and 2d that the wave

Table 1
Information in Figure 2

Signal label	Start time (s)	Ellipticity	Planarity	B amplitude (pT)	Polar k (°)	Polar p (°)
0′	0.22	0.86	0.96	5.12	157.2	167.6
1′	0.94	0.90	0.85	1.22	14.1	6.3
2′	1.85	0.81	0.66	0.92	145.9	152.3
3′	2.59	0.79	0.58	0.41	21.3	40.3
0	3.78	0.87	0.93	2.39	150.1	162.8
1	4.54	0.84	0.85	1.29	17.6	7.4
2	5.44	0.81	0.69	0.67	145.6	159.0
3	6.19	0.67	0.64	0.34	26.5	26.3

power tends to be weakened in the same series (e.g., wave power is the strongest for the signal labeled as 0 while is the weakest for the signal labeled as 3). During the same RBSPA passing, we identify 14 series from 37:19 (mm:ss) to 38:53 (mm:ss), each of which follows similar signal patterns of alternative wave normal angles. This complete set of 14 series are obtained from nine close waveforms and are shown in the supporting information.

We manually acquire the exact starting time of each 0.4 s Alpha signal pulse using the magnetic field power spectrum and the polar angle of the Poynting vector. The signal start times are labeled by the black dashed lines in Figure 2. Table 1 summarizes the median values of signal magnetic amplitude, wave normal angle and polar angle of Poynting vector for each identified signal during the 0.4 s signal time interval. The magnetic amplitude is calculated from the magnetic power spectrum over a bandwidth of 170Hz. Signal 0 and 0′ do not show clear temporal growth, but there are significant temporal growths in all the other signals. By manual inspections, the temporal growth rates of the signals are within the range of 60–120 dB/s. The signals do not strictly follow the guidance along the field line, which would yield 0° and 180° wave normal angles. Instead, the wave normal angles of the southward propagating signals are around 150°, while those of the northward propagating signals are around 20°.

Figures 2c and 2d also show the presence of triggered emissions with rising tones in the reflected signals 1′, 2′, 1, and 2, and falling tones in the reflected signals of the second sequence (1, 2, and 3). There is no triggered emission in the original signals labeled by 0′ or 0. The triggered emissions are generated after the observed original signals 0′ and 0 but before the observed first reflected signals 1′ and 1. For the 14 series of the same RBSPA passing, triggered emissions are present in all of the first reflected signals (signal 1, 1′, etc.) but in none of the original signals (signal 0, 0′, etc.). So, given the satellite location at MLAT = −6°, the interaction region where the triggered emissions are formed should be to the south of the satellite position instead of being located exactly at the equator.

4. Propagation Analysis

4.1. Propagation Time Estimate

To account for the gaps between the F_1 pulses with alternating propagation directions, we estimate the propagation time delay for reflected signals. Assuming the wave propagation does not deviate much from the field line, the time gaps between the signals in the same time series are estimated using

$$T = 2\int_{\lambda_{obs}}^{\lambda_{ref}} \frac{ds}{v_{gz}}, \tag{1}$$

where s is the length of the field line and $\lambda_{obs} = -6.0°$ is the observation latitude and $\lambda_{ref} = +43.2°$ (for the northward propagation) or −43.2° (for the southward propagation) is the latitude of the ionosphere at an assumed altitude of 100 km. The integral is done along the field line of the observation with $L = 1.91$. v_{gz} is the parallel component of the group velocity, which is calculated with the cold plasma dispersion relation. In the calculation, the cold electron density and the wave normal angle are assumed to be the same along the field line (Table 2). The observed time gaps are calculated from start times of the pulses listed in Table 1. Because there is no available density data exactly for the case (Figure 2b), we use linear interpolation of the logarithmic values of nearby density data within 20 min from the case. The interpolation result of $4.3 \times 10^3\,\mathrm{cm}^{-3}$ is within the range of 2.5–4.9 $\times 10^3\,\mathrm{cm}^{-3}$ for the equatorial density from a statistical density model at $L = 1.9$ based on IMAGE radio plasma imager data (Ozhogin et al., 2012). However, the use of interpolated density yields an estimate of the time gap which is about half of the observed values (Table 2). A larger value of plasma density is required to obtain a consistent propagation time estimate. The estimated arrival times become close to observations when the density is increased to $1.7 \times 10^4\,\mathrm{cm}^{-3}$ (Table 2). Such an increase of electron density above the background is also consistent with quasi-ducting of the pulse signals, which forms when there exists a density crest (Smith, 1961).

Table 2
Estimations of the Signal Time Gaps

Time gap	L shell	Density (cm^{-3})	WNA (°)	Observed time (s)	Estimated time (s)
$0' \sim 1'$ and $0 \sim 1$	1.9	4.3×10^3	25	0.74	0.34
$1' \sim 2'$ and $1 \sim 2$	1.9	4.3×10^3	25	0.91	0.50
$0' \sim 1'$ and $0 \sim 1$	1.9	1.7×10^4	25	0.74	0.67
$1' \sim 2'$ and $1 \sim 2$	1.9	1.7×10^4	25	0.91	0.99

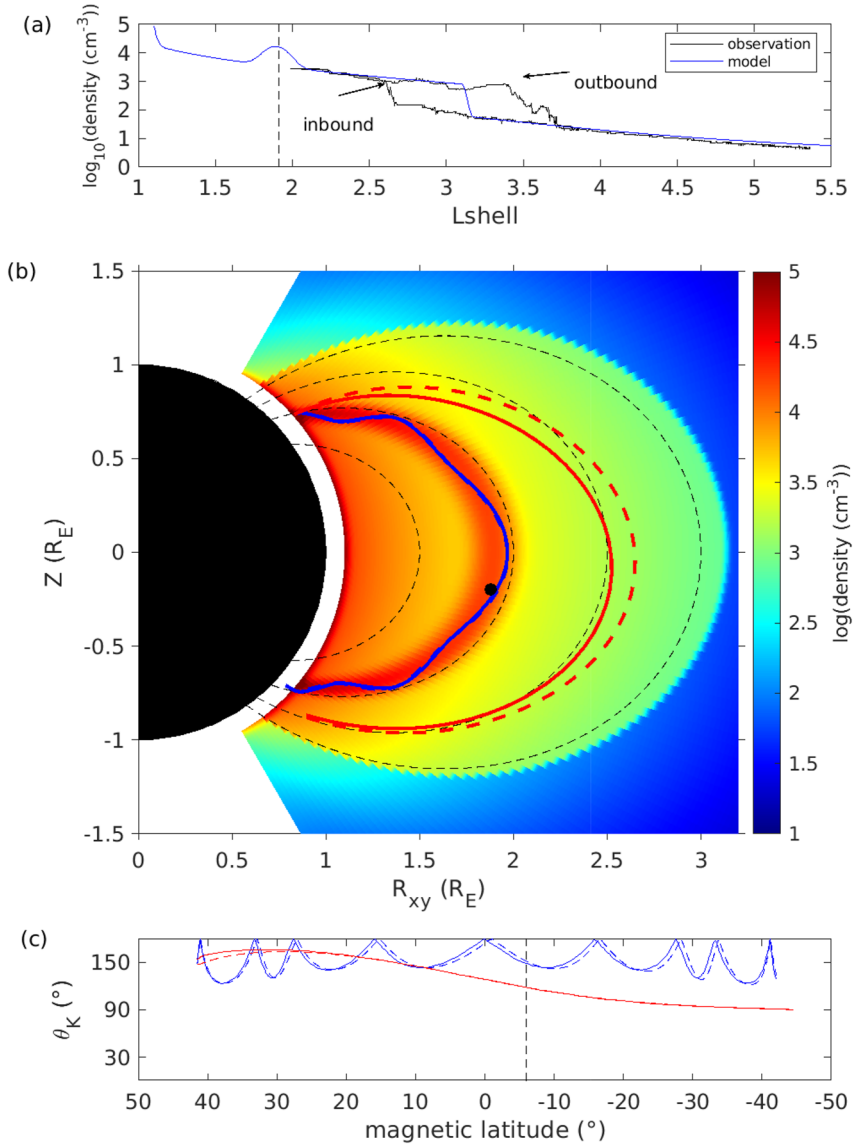

Figure 3. Ray tracing from Novosibirsk station. (a) Observed density profile within 2 h from the 14 November 2012 case (black) and equatorial density profile of the ray tracing model (blue). The black dashed line shows the L shell of the case. (b) Ray tracing of transmitter signals from NOV station. The two blue rays (solid and dashed) which overlap each other are from the edges of the ionospheric transmission cone in the meridional plane. Black dashed lines are the dipole magnetic field lines. Background electron density in the model is shown. The two red rays (sold and dashed) are launched with the same initial condition as the blue rays but in a background electron density model with the duct removed. The black dot shows the satellite location of the case. (c) The two blue lines show the wave normal angles of the two blue rays in subplot (b), while the red lines show the wave normal angles of the two red rays in subplot (b). The solid and dashed lines correspond to the solid and dashed lines in subplot (b), respectively. The two red lines overlap each other. The MLAT of the case is labeled by the black dashed line.

4.2. Ray Tracing

We conduct a ray tracing model, using the HOTRAY ray code (Horne, 1989) and a cold plasma density model by Bortnik et al. (2011). The density model consists of a diffusive equilibrium base and adjustable field-aligned structures (Bortnik et al., 2011). Guided by observed density profile (Figure 2b), the plasmapause is set at $L_{pp} = (2.7 + 3.5)/2 = 3.1$ with a width of $0.03R_E$. The plasmapause location is set as the average of the plasmapause locations of the inbound and outbound density profiles (black lines in Figure 3a). A density crest of density $1.7 \times 10^4\,\mathrm{cm}^{-3}$, which is suggested by the signal propagation time analysis, is added at the satellite position where $L = 1.9$. The density crest is Gaussian shaped with 300% increase of ambient density and a Gaussian width of $\Delta L = 0.1$. Figure 3a shows the comparison between the model's equatorial cold plasma density profile and two observed profiles (inbound and outbound). Initial locations of rays are set at 700 km altitude and at MLAT = 41.5° (corresponding to $L = 1.9$), which is within the coverage of F_1 frequency observations at NOV station by DEMETER at an altitude of 660 km (Zhang et al., 2017). Two rays are launched from the two edges of the transmission cone in the meridional plane at F_1 frequency, respectively. The transmission cone is calculated using a typical nighttime E layer electron number density of $5 \times 10^4\,\mathrm{cm}^{-3}$ (Zhang et al., 2018). The simulated raypaths, shown by the blue lines in Figure 3b, are ducted inside the density crest. The wave normal angles of the simulated ducted rays (the blue lines in Figure 3c) oscillate near 180° and get close to 150° at satellite's latitude (−6°) (Figure 3c), in accord with the observation. For comparison purpose, two nonducted rays are launched with the initial condition but in the density model with the density crest removed. Unlike ducted rays, the nonducted raypaths (red lines of Figure 3b) deviate significantly from the original field line. If undergoing magnetospheric reflection, those nonducted rays would spread the energy over a range of L shells (Kimura, 1966) and cannot reproduce reflected signals at the same field line as the observation shows. The wave normal angles of the nonducted rays are shown by red lines in Figure 3c. At satellite's latitude, the wave normal angle is near 120°, which is different from the observed values. Such comparison of the wave normal angles and raypaths of ducted and nonducted rays also support the observed case is in a ducted mode. The observed ducted propagation of Alpha transmitter signals at $L = 1.9$ agrees with previous studies that suggested existing ducted propagation at $L > 1.7$ (Agapitov et al., 2014; Cerisier, 1974; Ma et al., 2017).

5. Discussion on Triggered Emissions

5.1. Interaction Region

We use nonlinear cyclotron resonance theory to estimate the scale of interaction region in the event. The collective inhomogeneity factor S can be used to measure the interaction region (Omura et al., 2008):

$$S = -\frac{1}{\omega_t^2 \delta^2}\left\{\gamma\left(1 - \frac{v_r}{v_g}\right)^2 \frac{\partial \omega}{\partial t} + \left[\frac{k\gamma v_\perp^2}{2\Omega_e} - \left(1 + \frac{\delta^2}{2}\frac{\Omega_e - \gamma\omega}{\Omega_e - \omega}\right)v_r\right]\frac{\partial \Omega_e}{\partial s}\right\}, \tag{2}$$

where k is the wave vector and v_g is the wave group velocity. $v_\perp$ and $v_\parallel$ are the perpendicular and the parallel velocities of resonance electrons, respectively. The $\gamma = \left(1 - \frac{v_\perp^2 + v_\parallel^2}{c^2}\right)^{-1/2}$. $\delta^2 = 1 - \frac{\omega^2}{c^2 k^2}$. $\Omega_e = \frac{eB}{m_e}$ and B is the background magnetic field. The nonrelativistc trapping frequency is $\omega_t = \left(k v_\perp \frac{e}{m} B_w\right)^{1/2}$, and B_w is the wave magnetic field strength. The resonance frequency is $v_r = \frac{\omega - \Omega_e/\gamma}{k} \approx v_\parallel$. The interaction region requires $-1 < S < 1$ so the resonant electrons can be trapped in the phase space (Omura et al., 1991).

Here we assume parallel propagation of the transmitter signals and calculate k and v_g with cold plasma dispersion relation. $v_\parallel = v_r$ is set in the resonance condition. To better estimate the magnetic field minimum and the magnetic field gradient along the field line, the magnetic field line at the satellite's location is traced using IGRF 2000 model. The field minimum locates at MLAT = −1.87°. $\frac{\partial \omega}{\partial t} = 0$ is satisfied just before the wave triggering. In the 14 series, the wave amplitude ranges from 2 to 12 pT. We use the maximum amplitude $B_w = 12$ pT for the estimate. When electron pitch angle $\alpha = tan^{-1}\left(\frac{v_\perp}{|v_\parallel|}\right) = 62°$, the interaction region

reaches the southmost boundary at MLAT $= -3.1°$ $\left(\frac{\partial \Omega_e}{\partial s} = 1.1 \times 10^{-2}\,\mathrm{rad/m}\right)$ corresponding to $S = -1$. The observation of the transmitter signals in Figure 2, however, show that the triggering can occur southward of the satellite's location at MLAT $= -6°$ $\left(\frac{\partial \Omega_e}{\partial s} = 3.8 \times 10^{-2}\,\mathrm{rad/m}\right)$. Therefore, the simplified calculation underestimates the interaction region by a factor of 2 or so. In other words, the observed amplitude might be able to enable the interaction region larger than the estimate. A potential limitation about the above estimate is the neglect of $\partial\omega/\partial t$, which should be finite during the triggering process (Wu et al., 2020). Another limitation is that the current theory applies for the monochromatic wave of exact parallel propagation. As observation and ray tracing simulation shows, the ducted whistler waves can have small but finite inclination (25–35°) with respect to the background magnetic field. The transmitter signals are not exact monochromatic in that they are a series of pulses with a finite duration for each pulse. One can see in the observation, those trigger emissions tend to occur near the leading fronts of the pulses.

5.2. Chirping Rate

We manually inspect both the chirping rates of the falling tones and the rising tones. They fall in the range of 4–6 kHz/s. Because the satellite locates near the equator and close to the magnetic field minimum, we estimate the order of the chirping rate using the formula for equatorial rising tones by Omura et al. (2008):

$$\frac{\partial \omega}{\partial t} = 0.4\frac{\omega_t^2 \delta^2}{\gamma}\left(1 - \frac{v_r}{v_g}\right)^{-2}, \tag{3}$$

which assumes that the wave growth maximizes at $S = -0.4$. We choose $B_w = 12\,\mathrm{pT}$ and the same values as section 5.1 for other variables. The estimated chirping rate is 2.5 kHz/s, which is about half of the observed value. Such discrepancy of a factor of 2 between the observed and estimated sweep rates may suggest that the assumption of $S = -0.4$ may not always be a strict condition. In this context, Golkowski and Gibby (2017) suggest an S value of -0.86 may be dominant in the initial high growth phase of the nonlinear interaction that occurs downstream of the equator. Such a value would bring the sweep rate estimates very close to the observed one.

It has been suggested that the sign of the chirping rate (rising tones or falling tones) is related to the sign of inhomogeneity factor S (Nunn & Omura, 2012). At the equatorial upstream, where the signal is propagating from a higher latitude to the equator, the resonant electrons travel in the opposite direction from the equator. S goes from 0 to +1 (Omura et al., 1991) and the phase space trapping region contracts. Therefore, the phase space density increases and an electron hill may form, leading to the generation of falling tones (Nunn & Omura, 2012). Conversely, at the equatorial downstream where the signal is propagating away from the equator, S changes from -1 to 0 and rising tones can be generated by an electron hole (Omura et al., 2008). In the observation, we see rising tones followed by falling tones in the reflected signals at $-6°$ latitude close to the equator. The rising emissions might be triggered with the original reflected signal when they pass through the equatorial region. The falling tone may be triggered at equatorial upstream, when the reflected signal approaches the equator again. However, because traveling route from signal 0 to signal 1 consists both equatorial downstream and upstream, we cannot definitely test this hypothesis based on this event.

6. Conclusions

1. We perform an observation study of wave characteristics measured by the Van Allen Probes near the geomagnetic equator following emissions of Alpha transmitter signals at frequency $F_1 = 11.9$ kHz. The case shows multiple reflection signals with triggered emissions in the reflected signals. The signals have low wave normal angles 25–35°, corresponding to ducted propagation.
2. The time gaps between original and reflected signals are estimated using cold plasma dispersion relations. After adding a density crest, the estimated time gaps agree with the observations.
3. We estimate the interaction region length, as well as the order of value of the triggered emission chirping rate to test the nonlinear cyclotron resonance theory. The existing theory tends to underestimate the interaction length while the estimated chirping rate order is in accord with observations.

4. A ray tracing model shows ducted propagation with slightly oblique wave normal angle close to 150° at the satellite position in the presence of a local density crest, which is similar to the observed values. Without a density crest, the wave normal angle reaches 120°, far from the observed values. Therefore, we suggest that the signals propagate in a local density crest.

Data Availability Statement

The data of Van Allen Probes used in this paper are provided by Space Physics Data Facility (SPDF; https://spdf.gsfc.nasa.gov/).

Acknowledgments
We acknowledge the support of NSF grant AGS-1702805 and NASA grants 80NSSC19K0282 and NNX17AI52G.

References

Agapitov, O. V., Artemyev, A. V., Mourenas, D., Kasahara, Y., & Krasnoselskikh, V. (2014). Inner belt and slot region electron lifetimes and energization rates based on AKEBONO statistics of whistler waves. *Journal of Geophysical Research: Space Physics*, *119*, 2876–2893. https://doi.org/10.1002/2014JA019886

Bell, T. F., Inan, U. S., & Helliwell, R. A. (1981). Nonducted coherent VLF waves and associated triggered emissions observed on the ISEE-1 satellite. *Journal of Geophysical Research*, *86*(A6), 4649–4670. https://doi.org/10.1029/JA086iA06p04649

Bortnik, J., Chen, L., Li, W., Thorne, R. M., & Horne, R. B. (2011). Modeling the evolution of chorus waves into plasmaspheric hiss. *Journal of Geophysical Research*, *116*, A08221. https://doi.org/10.1029/2011JA016499

Carpenter, D. L., & Miller, T. R. (1976). Ducted magnetospheric propagation of signals from the Siple, Antarctica, VLF transmitter. *Journal of Geophysical Research*, *81*(16), 2692–2700. https://doi.org/10.1029/JA081i016p02692

Cerisier, J. (1973). A theoretical and experimental study of non-ducted VLF waves after propagation through the magnetosphere. *Journal of Atmospheric and Terrestrial Physics*, *35*(1), 77–94. https://doi.org/10.1016/0021-9169(73)90217-1

Cerisier, J. (1974). Ducted and partly ducted propagation of VLF waves through the magnetosphere. *Journal of Atmospheric and Terrestrial Physics*, *36*(9), 1443–1467. https://doi.org/10.1016/0021-9169(74)90224-4

Clilverd, M. A., Rodger, C. J., Gamble, R., Meredith, N. P., Parrot, M., Berthelier, J. J., & Thomson, N. R. (2008). Ground-based transmitter signals observed from space: Ducted or nonducted? *Journal of Geophysical Research*, *113*, A04211. https://doi.org/10.1029/2007JA012602

Edgar, B. (1972). Structure of the magnetosphere as deduced from magnetospherically reflected whistlers. Stanford, Calif., Radiosc. Lab., Stanford Electron. Lab., Stanford Univ.

Golkowski, M., & Gibby, A. R. (2017). On the conditions for nonlinear growth in magnetospheric chorus and triggered emissions. *Physics of Plasmas*, *24*(9), 092904. https://doi.org/10.1063/1.4986225

Golkowski, M., Harid, V., & Hosseini, P. (2019). Review of controlled excitation of non-linear wave-particle interactions in the magnetosphere. *Frontiers in Astronomy and Space Sciences*, *6*, 2. https://doi.org/10.3389/fspas.2019.00002

Golkowski, M., Inan, U. S., Cohen, M. B., & Gibby, A. R. (2010). Amplitude and phase of nonlinear magnetospheric wave growth excited by the HAARP HF heater. *Journal of Geophysical Research*, *115*, A00F04. https://doi.org/10.1029/2009JA014610

Harid, V., Golkowski, M., Bell, T., Li, J. D., & Inan, U. S. (2014). Finite difference modeling of coherent wave amplification in the Earth's radiation belts. *Geophysical Research Letters*, *41*, 8193–8200. https://doi.org/10.1002/2014GL061787

Helliwell, R. A. (1965). Whistlers and related ionospheric phenomena. Stanford University Press.

Helliwell, R. A., & Katsufrakis, J. P. (1974). VLF wave injection into the magnetosphere from Siple Station, Antarctica. *Journal of Geophysical Research*, *79*(16), 2511–2518. https://doi.org/10.1029/JA079i016p02511

Hikishima, M., Omura, Y., & Summers, D. (2010). Self-consistent particle simulation of whistler mode triggered emissions. *Journal of Geophysical Research*, *115*, A12246. https://doi.org/10.1029/2010JA015860

Horne, R. B. (1989). Path-integrated growth of electrostatic waves: The generation of terrestrial myriametric radiation. *Journal of Geophysical Research*, *94*(A7), 8895–8909. https://doi.org/10.1029/JA094iA07p08895

Jacobsen, T. (2006). The Russian VLF Navaid System, Alpha, RSDN-20. https://www.vlf.it/alphatrond/alpha.htm

Kimura, I. (1966). Effects of ions on whistler-mode ray tracing. *Radio Science*, *1*(3), 269–284. https://doi.org/10.1002/rds196613269

Kimura, I., Kasahara, Y., & Oya, H. (2001). Determination of global plasmaspheric electron density profile by tomographic approach using omega signals and ray tracing. *Journal of Atmospheric and Solar-Terrestrial Physics*, *63*(11), 1157–1170. https://doi.org/10.1016/S1364-6826(00)00220-0

Kirby, K., Artis, D., Bushman, S., Butler, M., Conde, R., Cooper, S., & Williams, B. (2014). Radiation Belt Storm Probes—Observatory and environments. In N. Fox, & J. L. Burch (Eds.), *The Van Allen Probes mission* (pp. 59–125). Boston, MA: Springer US. https://doi.org/10.1007/978-1-4899-7433-4_4

Kletzing, C. A., Kurth, W. S., Acuna, M., MacDowall, R. J., Torbert, R. B., Averkamp, T., & Tyler, J. (2013). The Electric and Magnetic Field Instrument Suite and Integrated Science (EMFISIS) on RBSP. *Space Science Reviews*, *179*(1), 127–181. https://doi.org/10.1007/s11214-013-9993-6

Koronczay, D., Lichtenberger, J., Juhsz, L., Steinbach, P., & Hospodarsky, G. (2018). VLF transmitters as tools for monitoring the plasmasphere. *Journal of Geophysical Research: Space Physics*, *123*, 9312–9324. https://doi.org/10.1029/2018JA025802

Kulkarni, P., Gokowski, M., Inan, U. S., & Bell, T. F. (2015). The effect of electron and ion temperature on the refractive index surface of 1–10 kHz whistler mode waves in the inner magnetosphere. *Journal of Geophysical Research: Space Physics*, *120*, 581–591. https://doi.org/10.1002/2014JA020669

Kurth, W. S., De Pascuale, S., Faden, J. B., Kletzing, C. A., Hospodarsky, G. B., Thaller, S., & Wygant, J. R. (2015). Electron densities inferred from plasma wave spectra obtained by the Waves instrument on Van Allen Probes. *Journal of Geophysical Research: Space Physics*, *120*, 904–914. https://doi.org/10.1002/2014JA020857

Li, J. D., Spasojevic, M., & Inan, U. S. (2015). An empirical profile of VLF triggered emissions. *Journal of Geophysical Research: Space Physics*, *120*, 6581–6595. https://doi.org/10.1002/2015JA021444

Ma, Q., Mourenas, D., Li, W., Artemyev, A., & Thorne, R. M. (2017). VLF waves from ground-based transmitters observed by the Van Allen Probes: Statistical model and effects on plasmaspheric electrons. *Geophysical Research Letters*, *44*, 6483–6491. https://doi.org/10.1002/2017GL073885

Means, J. D. (1972). Use of the three-dimensional covariance matrix in analyzing the polarization properties of plane waves. *Journal of Geophysical Research*, *77*(28), 5551–5559. https://doi.org/10.1029/JA077i028p05551

Nunn, D., & Omura, Y. (2012). A computational and theoretical analysis of falling frequency VLF emissions. *Journal of Geophysical Research*, *117*, A08228. https://doi.org/10.1029/2012JA017557

Omura, Y., Katoh, Y., & Summers, D. (2008). Theory and simulation of the generation of whistler-mode chorus. *Journal of Geophysical Research*, *113*, A04223. https://doi.org/10.1029/2007JA012622

Omura, Y., Nunn, D., Matsumoto, H., & Rycroft, M. (1991). A review of observational, theoretical and numerical studies of VLF triggered emissions. *Journal of Atmospheric and Terrestrial Physics*, *53*(5), 351–368. https://doi.org/10.1016/0021-9169(91)90031-2

Ozhogin, P., Tu, J., Song, P., & Reinisch, B. W. (2012). Field-aligned distribution of the plasmaspheric electron density: An empirical model derived from the IMAGE RPI measurements. *Journal of Geophysical Research*, *117*, A06225. https://doi.org/10.1029/2011JA017330

Rastani, K., Inan, U. S., & Helliwell, R. A. (1985). DE 1 observations of siple transmitter signals and associated sidebands. *Journal of Geophysical Research*, *90*(A5), 4128–4140. https://doi.org/10.1029/JA090iA05p04128

Santolík, O., Parrot, M., & Lefeuvre, F. (2003). Singular value decomposition methods for wave propagation analysis. *Radio Science*, *38*(1), 1010. https://doi.org/10.1029/2000RS002523

Smith, R. L. (1961). Propagation characteristics of whistlers trapped in field-aligned columns of enhanced ionization. *Journal of Geophysical Research*, *66*(11), 3699–3707. https://doi.org/10.1029/JZ066i011p03699

Sonwalkar, V. S., & Inan, U. S. (1986). Measurements of Siple transmitter signals on the DE 1 satellite: Wave normal direction and antenna effective length. *Journal of Geophysical Research*, *91*(A1), 154–164. https://doi.org/10.1029/JA091iA01p00154

Tanaka, Y., Lagoutte, D., Hayakawa, M., Lefeuvre, F., & Tajima, S. (1987). Spectral broadening of VLF transmitter signals and sideband structure observed on Aureol 3 satellite at middle latitudes. *Journal of Geophysical Research*, *92*(A7), 7551–7559. https://doi.org/10.1029/JA092iA07p07551

Tanaka, Y., Nishino, M., & Hayakawa, M. (1987). Conjugate measurements of VLF transmitter signals at middle latitude (L = 1.93). *Planetary and Space Science*, *35*(8), 1053–1059. https://doi.org/10.1016/0032-0633(87)90009-2

Tao, X., Zonca, F., Chen, L., & Wu, Y. (2020). Theoretical and numerical studies of chorus waves: A review. *Science China Earth Sciences*, *63*, 78–92. https://doi.org/10.1007/s11430-019-9384-6

Vavilov, D., Shklyar, D., Titova, E., & Parrot, M. (2013). Study of the lower hybrid resonance frequency over the regions of gathering earthquakes using DEMETER data. *Journal of Atmospheric and Solar-Terrestrial Physics*, *100–101*, 1–12. https://doi.org/10.1016/j.jastp.2013.03.019

Wang, G., & Berk, H. (2012). Simulation and theory of spontaneous TAE frequency sweeping. *Nuclear Fusion*, *52*(9), 094003. https://doi.org/10.1088/0029-5515/52/9/094003

Wu, Y., Tao, X., Zonca, F., Chen, L., & Wang, S. (2020). Controlling the chirping of chorus waves via magnetic field inhomogeneity. *Geophysical Research Letters*, *47*, e2020GL087791. https://doi.org/10.1029/2020GL087791

Wygant, J., Bonnell, J., Goetz, K., Ergun, R., Mozer, F., Bale, S., & Tao, J. (2013). The Electric Field and Waves instruments on the Radiation Belt Storm Probes mission. *Space Science Reviews*, *179*(1–4), 183–220. https://doi.org/10.1007/s11214-013-0013-7

Yamaguchi, K., Matsumuro, T., Omura, Y., & Nunn, D. (2013). Ray tracing of whistler-mode chorus elements: Implications for generation mechanisms of rising and falling tone emissions. *Annales Geophysicae*, *31*(4), 665–673. https://doi.org/10.5194/angeo-31-665-2013

Yamamoto, M., Ito, Y., Kishi, Y., Sawada, A., Kimura, I., Nagano, I., & Hashimoto, K. (1991). k vector measurements of VLF signals by the satellite EXOS-D. *Geophysical Research Letters*, *18*(2), 325–328. https://doi.org/10.1029/91GL00031

Zhang, Z., Chen, L., Li, X., Xia, Z., Heelis, R. A., & Horne, R. B. (2018). Observed propagation route of VLF transmitter signals in the magnetosphere. *Journal of Geophysical Research: Space Physics*, *123*, 5528–5537. https://doi.org/10.1029/2018JA025637

Zhang, X., Zhao, S. F., Ruzhin, Y., Liu, J., & Song, R. (2017). The spatial distribution features of three Alpha transmitter signals at the topside ionosphere. *Radio Science*, *52*, 653–662. https://doi.org/10.1002/2016RS006219